
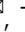




Scalable fabrication of graphene nanoribbon quantum dot devices with stable orbital-level spacing

Toshiaki Kato ^{1,7}, Takahito Kitada^{1,2,7}, Mizuki Seo¹, Wakana Okita¹, Naofumi Sato¹, Motoya Shinozaki^{1,2}, Takaya Abe^{1,2}, Takeshi Kumasaka², Takumi Aizawa^{1,2}, Yui Muto^{1,2}, Toshiro Kaneko¹ & Tomohiro Otsuka^{1,2,3,4,5,6,7}

Large-scale integration of quantum-dot devices is essential for realizing various quantum devices. Graphene-based quantum dots provide a promising platform for spin qubits because of their low nuclear spin density and weak spin-orbit interaction. However, the integration of graphene-based quantum dots remains a challenge. Here, we demonstrate the scalable fabrication of graphene nanoribbon-based quantum-dot devices using a nickel nanobar technique. Fine structures formed in the middle of the nanoribbons exhibit quantum-dot behavior, and more than 56% of devices fabricated on the same substrate show Coulomb diamond features, indicating that large-scale integration of graphene nanoribbon quantum-dot devices is possible with our method. Cryogenic measurements reveal orbital-level spacings between the ground and excited states that are stable up to high-temperature conditions of ~20 K. We explain this stability in terms of the very fine structures formed in the middle of the nanoribbons and their relatively low effective mass.

¹ Graduate School of Engineering, Tohoku University, Aoba 6-6-05, Aramaki, Aoba-ku, Sendai 980-8579, Japan. ² Research Institute of Electrical Communication, Tohoku University, 2-1-1 Katahira, Aoba-ku, Sendai 980-8577, Japan. ³ WPI Advanced Institute for Materials Research, Tohoku University, Sendai 980-8577, Japan. ⁴ Center for Emergent Matter Science, RIKEN, 2-1 Hirosawa, Wako, Saitama 351-0198, Japan. ⁵ Center for Spintronics Research Network, Tohoku University, 2-1-1 Katahira, Aoba-ku, Sendai 980-8577, Japan. ⁶ Center for Science and Innovation in Spintronics, Tohoku University, 2-1-1 Katahira, Aoba-ku, Sendai 980-8577, Japan. ⁷ These authors contributed equally: Toshiaki Kato, Takahito Kitada, Tomohiro Otsuka. email: kato12@tohoku.ac.jp; tomohiro.otsuka@tohoku.ac.jp

Graphene-based quantum dots (QDs) provide a promising platform for spin qubits, which can have long spin coherence times because of their low nuclear spin density and weak spin-orbit interaction^{1–3}. Graphene-based QD devices can be fabricated by the simple etching of two-dimensional (2D) monolayer graphene^{4–6} and local-gate controlled bi-layer graphene with perpendicular electric fields⁷. Narrow and short graphene nanoribbons (GNRs) can be also used as QD devices^{8–10}. Several fundamental features, such as electron-hole crossover¹¹, the excitation spectrum⁶, spin and valley states¹², and charge relaxation times¹³, have been reported, indicating the potential abilities of graphene-based QD devices. Despite these promising fundamental studies, the use of graphene-based QDs in real applications is yet to be realized. One of the critical subjects for further investigation is integration. Large-scale integration of QD devices is essential for realizing quantum computing^{14,15}, sensors^{16–18}, and other devices¹⁹. However, the integration of graphene-based QDs remains a challenge^{20,21}. The lack of scalability of current fabrication processes is a critical barrier preventing this research field from further development toward commercial use, as has been demonstrated for Si and GaAs QD devices^{22–24}.

We previously developed a unique method for the site- and alignment-controlled synthesis of GNRs²⁵. Through the use of Ni nanobars and advanced plasma processing, high-yield synthesis of 1,000,000 GNRs has been realized at the wafer scale²⁶. Non-volatile memory operation based on persistent photoconductivity and enhanced thermoelectric performance have also been demonstrated with our highly-integrated GNRs^{27,28}. Although this scalable fabrication process possesses a potential for the practical use of graphene-based QD devices, detailed-quantum features have not been investigated because of the relatively long GNR length ($\sim 1 \mu\text{m}$).

We modified our scalable GNR fabrication method for the synthesis of QDs, and the efficient synthesis of GNR-based QD devices was realized with accurate site controllability through adjustment of the Ni nanobar length and growth conditions. Furthermore, a clear orbital-level spacing between the ground state (GS) and excited state (ES) is observed in our GNR-based QD device. Surprisingly, the orbital-level spacings were stable even at 20 K, which is much higher than that of a QD device composed of Si and GaAs (up to $\sim 1 \text{ K}$ ²⁹). These scalable QD devices with high-temperature stability will strongly contribute to the next stage of the development of graphene-based QDs.

Results and discussion

Fabrication of GNR-based QD device. GNR growth was performed using a homemade plasma chemical vapor deposition (CVD) system^{25,26}. Detailed information can be found in the Methods section. Most of the GNR-QDs used in our studies are not monolayer but multi-layer, which was confirmed by Raman scattering spectra (Supplementary Fig. 1). The electrical transport properties were measured using a low-temperature probe station ($\sim 15 \text{ K}$) (“15 K system”) and He-pumping refrigerator ($\sim 2.2 \text{ K}$) (“2.2 K system”), in which systematic measurements for many devices with moderate resolution and high-resolution measurements for specific devices were possible, respectively. In this study, more than 100 devices were fabricated by varying the growth conditions and nanobar lengths (Fig. 1a). The features observed in our devices can be divided into several categories (Fig. 1b–e). The first selection is related to Coulomb blockade (CB) (Fig. 1b, c). A CB can be identified from a drain-source current (I_{ds}) versus a drain-source voltage (V_{ds}) curve under a specific gate bias (V_{g}). If the $I_{\text{ds}}-V_{\text{ds}}$ curve shows linear features or a continuous off-current region, these devices can be identified as

No-CB (Fig. 1b) or CB (Fig. 1c) devices, respectively. There are two different sub-categories of CB devices: Coulomb diamond (CD) (Fig. 1d) and No-CD (Fig. 1e) devices, as determined by the shape of the off-current region, i.e., depending on whether diamond-like shapes can be observed. For CD devices, there is a critical difference in the appearance of the ES (Fig. 1f, g). The ES can appear as parallel lines on the edge (GS) of CD (Fig. 1g). The appearance of the ES indicates that the orbital-level spacing is sufficient to identify the up- and down-spin levels due to Zeeman splitting under a magnetic field (Fig. 1g). The up- and down-spin states provide information about the spin qubits in quantum devices. Thus, obtaining QD devices with clear orbital-level spacings between the GS and ES or ES and ES is very important for the realization of spin-qubit applications.

Based on these systematic investigations, it was determined that the Ni nanobar length (L_{Ni}) is a critical factor in determining the quantum transport properties of GNRs. First, we focused on the device fabrication yield (Y_{d}), which is the percentage of devices in which the on-current at $V_{\text{ds}} = 100 \text{ mV}$ was greater than 100 pA. In the case of short L_{Ni} , Y_{d} reached $\sim 90\%$ and clearly decreased when L_{Ni} was $\geq 200 \text{ nm}$ (Fig. 2a). This can be correlated to the unique growth mode of our GNR device (discussed further below). The quantum transport properties also showed an obvious dependence on L_{Ni} ; the CB appearance rate increased with longer L_{Ni} (Fig. 2b). These Y_{d} and CB trends can be explained as follows: a low Y_{d} indicates that most of the Ni nanobars are broken during the CVD process. However, just before a Ni nanobar is broken, very fine structures called “break points” (BP) are formed. If the GNR can be nucleated from such BPs, a fine GNR may be formed from a relatively long L_{Ni} , resulting in the frequent occurrence of CBs.

Further detailed analyses were performed to prove the accuracy of this hypothesis. The contribution of the fine GNR structures to the occurrence of CBs can also be determined from the conductance (G) vs. on/off plot, where G is normalized by the quantum conductance (G_0). Because the bandgap of a GNR is related to its width, it can be conjectured that the on/off ratio increases when a fine structure is formed within the GNR. When the room temperature on/off ratio was low, CBs were not observed—even at low temperatures (Fig. 2d). In contrast, for a relatively high on/off ratio, CBs were frequently observed (Fig. 2d), indicating that the formation of a fine structure in the GNR is directly correlated with the appearance of CBs. In this study, most GNR device exhibit on/off ratios of 1–100 (Fig. 2d), which is lower than that fabricated by other methods. This can be explained by the multi-layer dominant structure of our GNR.

For CB to occur, not only a fine structure but also a large contact barrier is required. The contact barrier height was estimated as the activation energy (E_{a}) from the temperature dependence of the minimum conductance (G_{min}) of the No-CB and CB devices. For a No-CB device, E_{a} is approximately 5.3 meV (Fig. 2e), which can be attributed to the contact barrier between the Ni electrode and the GNR. The E_{a} of a GNR device with a CB is approximately 218 meV (Fig. 2f), which is more than 40 times greater than that of a No-CB device, indicating that a sufficient contact barrier is formed in a CB device.

The correlation between the fine structure of GNRs and the appearance of CBs can be rationalized as follows. CB devices can be classified as either CD or No-CD devices (Fig. 1d, e, respectively). For an L_{Ni} of 100–200 nm, the CD device becomes dominant, whereas a longer L_{Ni} enhances the formation of a No-CD device (Fig. 2c). This L_{Ni} dependence could be related to the number of fine structures within the GNR. A nanobar with a longer L_{Ni} can form multiple fine structures, resulting in a decrease in Y_{d} (Fig. 2a) and promotion of QD formation, resulting in No-CD (Fig. 2c). When plotting the room

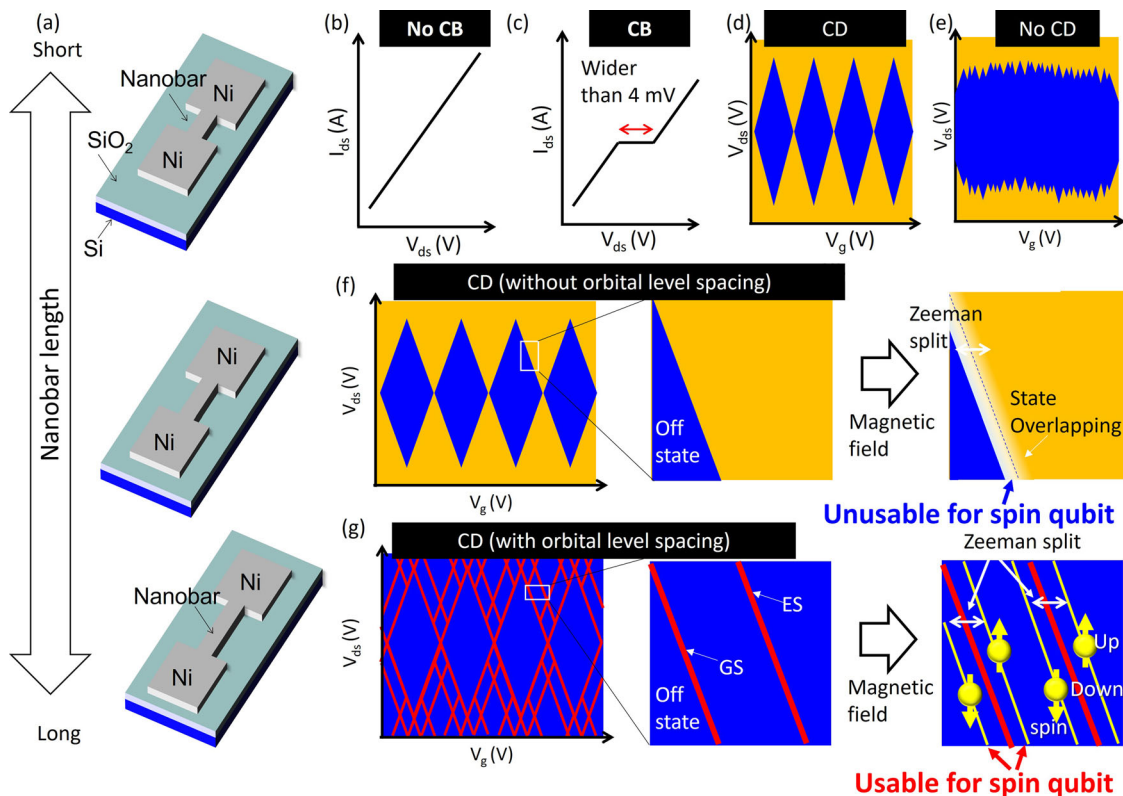


Fig. 1 Schematic illustration of GNR fabrication and categorization of quantum features. **a** Device structure with different L_{Ni} values. **b–e** Categorization of device features for **b** No-CB, **c** CB, **d** CD, and **e** No-CD devices. **f, g** Difference of CD device **f** without and **g** with orbital-level spacing.

temperature resistance (R_T) of GNRs in No-CB devices, the R_T values of the CD and No-CD devices were in different ranges (Fig. 2g). The R_T values of all the No-CB devices were below 100 k Ω , while those of CD and No-CD devices were in the ranges of 10^2 – 10^4 and 10^5 – 10^7 k Ω , respectively (Fig. 2g). These R_T differences between the CD and No-CD devices can be explained by the variation in the number of fine structures within a single GNR channel. It can be assumed that each fine structure has a relatively similar R_T order, and No-CD devices can be seen as a series connection of these fine structures (Supplementary Fig. 2).

As shown in Fig. 2c, a CD device became dominant for L_{Ni} in the range of 100–200 nm. It can be conjectured that the unique growth mechanism of GNRs from Ni nanobars played an important role in explaining this result²⁶. In a previous study, we demonstrated that Ni nanobars have a liquid phase during CVD that breaks into two pieces after the segregation of GNRs²⁶. Droplets of Ni nanobars move in opposite directions along the GNR axis owing to capillary forces, resulting in the formation of suspended GNRs. The breaking of liquid-phase Ni can be explained by the Plateau-Rayleigh (PR) instability arising within liquid-phase Ni nanobars²⁶. The calculated wavelength of PR instability (λ_{PR}) was approximately 100 nm (Supplementary Fig. 3). This implies that when L_{Ni} is a few multiples of λ_{PR} , a few QDs are formed (Fig. 2c). Thus, it is expected that the fine structure formation in GNRs is directly correlated with the BPs of liquid-phase Ni that may arise at the node point of the PR instability wave (Fig. 2h and S3). If GNR nucleation occurs during the breaking of liquid-phase Ni, a very fine structure of the GNRs can be formed. Therefore, a fine structure, considered to be the origin of quantum features within our GNR, may be formed at the node point of the PR instability arising in liquid-phase Ni.

To support this hypothesis, we performed a direct comparison between quantum features and the GNR structure. When we

observed the shape of the GNRs, which showed a clear CD (Fig. 2i), a very fine structure was formed in the middle of the GNR (Fig. 2j). This finding is consistent with the explanation discussed above.

Integration of GNR-based QD devices. Large-scale integration is critical for the use of QDs as quantum devices. Because L_{Ni} = 100–200 nm shows the highest probability of CD device fabrication (Fig. 2c), large-scale integrations were carried out with a suitable device geometry (L_{Ni} = 200 nm). The 16 GNR devices were designed within the same substrate (~ 10 mm \times 10 mm) (Fig. 3a) and the stability diagram was measured for each. Noticeably, nine devices exhibited CD features (Fig. 3b), indicating that the fabrication yield of the quantum GNR device with CD features was greater than 56%. As our approach is scalable, further large-scale integration of GNR-QD devices is possible.

Controlling the state of carriers in QDs is also important and can be achieved with a side-gate operation (Fig. 3a, c). It should be noted that the side-gate patterns were initially formed together with the Ni nanobars and other electrodes. Thus, a side-gate device can be fabricated without post-processing for electrode formation, i.e., a clean as-grown surface of the GNR can be maintained during the measurement of quantum features. In both sweeps of side gate1 (sg1) and side gate2 (sg2), a similar Coulomb oscillation was observed (Fig. 3d, e). When we measured I_{ds} as a function of sg1 and sg2, clear straight-line patterns were obtained, indicating that carriers confined within GNR-QDs can be well controlled by side gates (Fig. 3f). Similar side-gate operations can also be realized using other devices (Supplementary Figs. 4, 5). Furthermore, the carrier state within a GNR-QD can be quickly switched by applying V_0 and V_1 to sg1 (Fig. 3g, h, respectively), indicating that the quantum state in the GNR is very stable

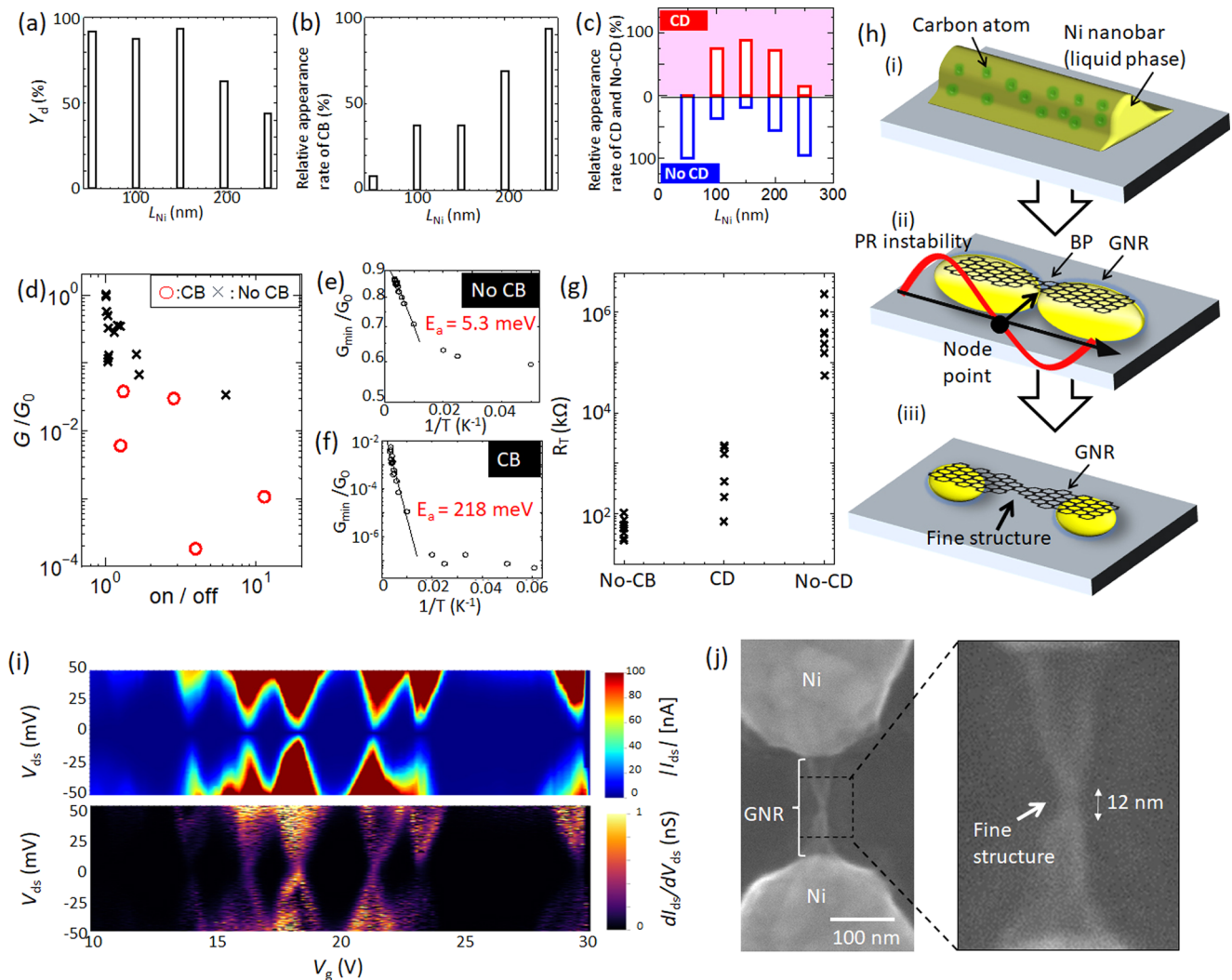


Fig. 2 Efficient fabrication of GNR-based QD devices. **a–c** L_{Ni} dependence of **a** Y_d , relative appearance rate of **b** CB, and **c** (red) CD and (blue) No-CD devices. **d** Plot of G/G_0 vs. on/off ratio (room temperature) for CB (O) and No-CB (x) devices. **e, f** Arrhenius plot of G_{min}/G_0 for **e** No-CB and **f** CB device. **g** Plot of R_T for No-CB, single-like dot, and multi-dot devices. **h** Typical model of correlation between λ_{PR} and fine structure in GNR (i, state of Ni nanobar just before segregation of GNRs; ii, after segregation of GNRs from Ni nanobar with a BP at the nose point of the PR instability wave; iii, GNR with fine structure). **i** Typical (top) I_{ds} and (bottom) $dI_{\text{ds}}/dV_{\text{ds}}$ mapping as functions of V_g and V_{ds} for a CD device. **j** (left) Low and (right) high magnification SEM images of the GNR device used for (i).

without any hysteresis, which may be useful for various quantum applications.

Detailed-quantum features in GNR-based QD device. As mentioned above, for the application of QD devices as spin qubits, control of the carrier and spin state is important. To address this issue, maintaining a sufficiently large orbital-level spacing is critical (Fig. 1g). To confirm the possibility of spin-qubit application of our GNR-QD device, further detailed measurements of the quantum features were carried out at cryogenic temperatures (~ 2.2 K). Large CDs with $\Delta V_{\text{ds}} \sim 100$ mV were observed with closed shapes at zero bias, indicating the formation of a single QD (Fig. 4a). Outside the CDs (GS), ESs parallel to the edges of the diamonds were also observed, demonstrating that a large orbital-level spacing between the GS and ES was maintained in our GNR device. These ESs correspond to the orbitals in the QD formed by size quantization. Similar transport properties were also observed in other devices, as shown in Fig. 4b, c. It should be noted that the density of state in graphene lead can be modulated by V_g , which can show multiple lines outside of CD

regions³⁰. However, those lines are known to be shown as non-parallel lines to the edge of the CD. Therefore, parallel lines observed in this study should be coming from not a lead state but ES.

Figure 5 shows the temperature dependence of the transport properties (Fig. 5a:2.2 K, 5b:20 K, 5c:50 K, and 5d:80 K). With increasing temperature, the ES and CBs became blurred because of the broadening of the electron energy distribution in the leads. The ESs disappeared at 50 K, and CDs were maintained up to ~ 80 K (Fig. 5a–d). We analyzed the width of the ES by varying the temperature. Figure 5e shows the current peak at the ES in Device 2 (Fig. 4b). The peak width increased with increasing temperature. The peak width (σ) at $V_{\text{ds}} \approx 0.15$ V was extracted by Gaussian fitting and is plotted as a function of temperature in Fig. 5f. The width increased linearly, indicating that peak broadening due to the tunneling rate was less than that due to temperature. From the slope of the linear fit, the conversion factor was evaluated as $\alpha = 2.75$, which describes the real V_{ds} applied through the quantum dot $V_{\text{ds, dot}} = V_{\text{ds}} / \alpha$ around this ES. α is induced by in-series resistive components in the GNR and at the

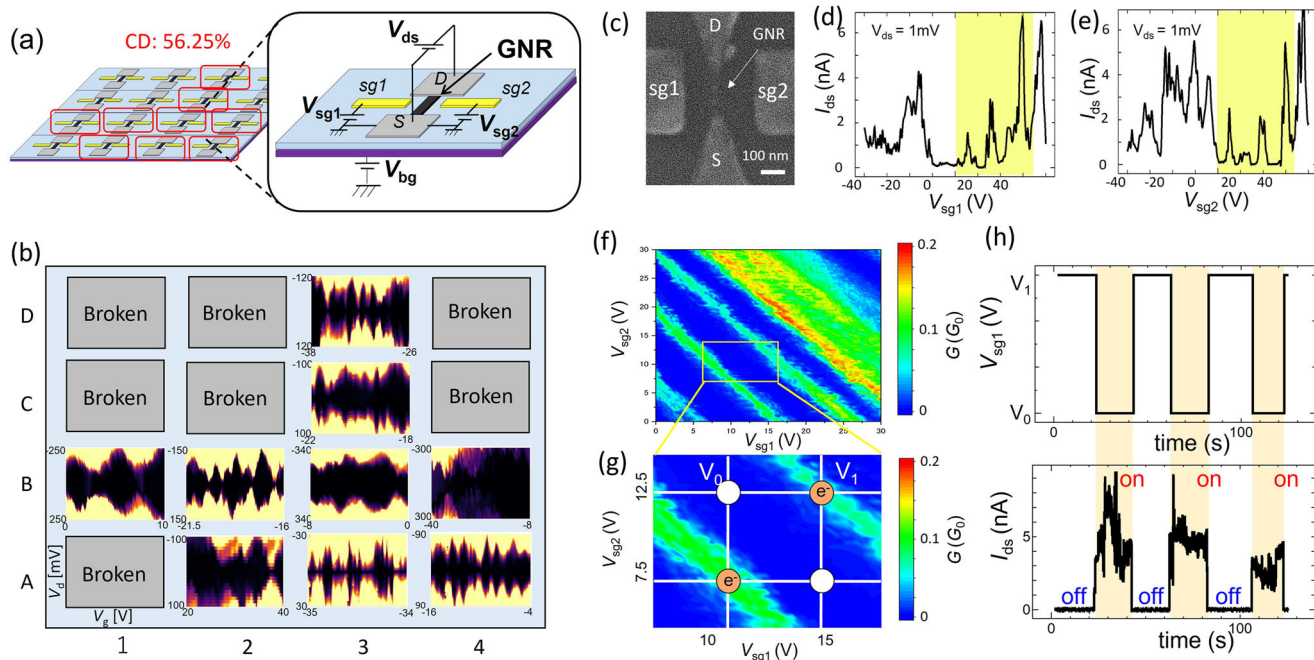


Fig. 3 Site-controlled fabrication of integrated GNR-based QD devices. **a** Typical illustration of device patterns and detailed device structures. **(b)** All 16 GNR-device features measured at 15 K were fabricated within the same substrate. **c** Typical SEM image and **d, e** Coulomb oscillation features of GNR-based QD devices operated by **d** sg1 and **e** sg2. Contour plot of G/G_0 as functions of V_{sg1} and V_{sg2} swept in **f** wide and **g** narrow ranges. **h** (top) Time profile of V_{sg1} switched between V_0 and V_1 and (bottom) its I_{ds} response.

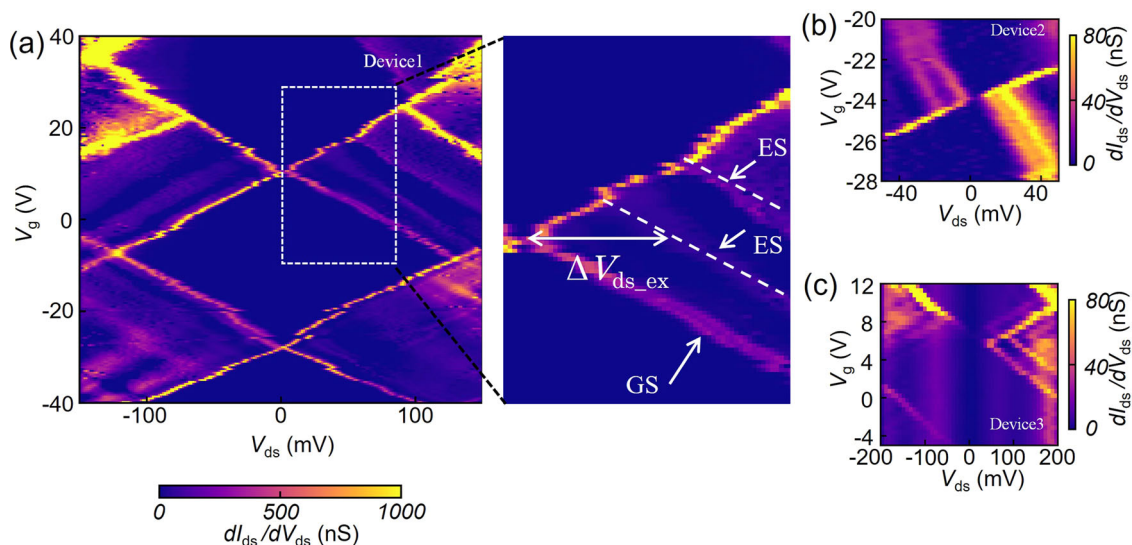


Fig. 4 GS and ES of CDs in our GNR device. **a-c** Typical Coulomb diamonds with GS and ES lines measured at 2.2 K for various GNR devices (**a** Device 1, **b** Device 2, and **c** Device 3).

interface between the GNR and metal³¹. From the stability diagram in Fig. 4b, the charging energy corresponds to $E_c = \Delta V_{ds,c} = 25$ mV and the excited-level spacing is $\Delta V_{ds,ex} = 13$ mV. The excited-level spacing can be calibrated by α , resulting in $E_{ex} = \Delta V_{ds,ex}/2.75 = 5.1$ meV. These results are consistent with the temperature dependence shown in Fig. 5.

We estimated the dot size using a capacitance model²⁶. The area of dot A was calculated as follows:

$$A = \frac{w}{d_0 + d_1} \cdot \frac{C_g}{CE_c} \left(\frac{d_0}{\epsilon_0} + \frac{d_1}{\epsilon_1} \right)$$

where d_0 is the distance between the GNR and wafer surface, d_1 is the SiO₂ thickness, ϵ_0 is the permittivity of a vacuum, ϵ_1 is the

permittivity of SiO₂, w is the GNR width, C_g is the capacitance of the gate, and C is the overall capacitance of the dot. Using this equation, the dot size was estimated to be 14 nm². This size is much smaller than that of the entire GNR geometry, indicating that the dot is locally formed inside the GNR, as discussed previously.

We now discuss why the orbital-level spacing in our GNR was stable under high-temperature conditions (~ 20 K). To observe the ES under high-temperature conditions, $\Delta V_{ds,ex}$ must be larger than the thermal energy. $\Delta V_{ds,ex}$ is inversely proportional to the multiple of a carrier (electron or hole) effective mass (m^*) and area of the QD (A) ($\Delta V_{ds,ex} \propto \hbar^2/m^*A$). Thus, smaller dots with lighter m^* are ideal candidates for increasing the threshold

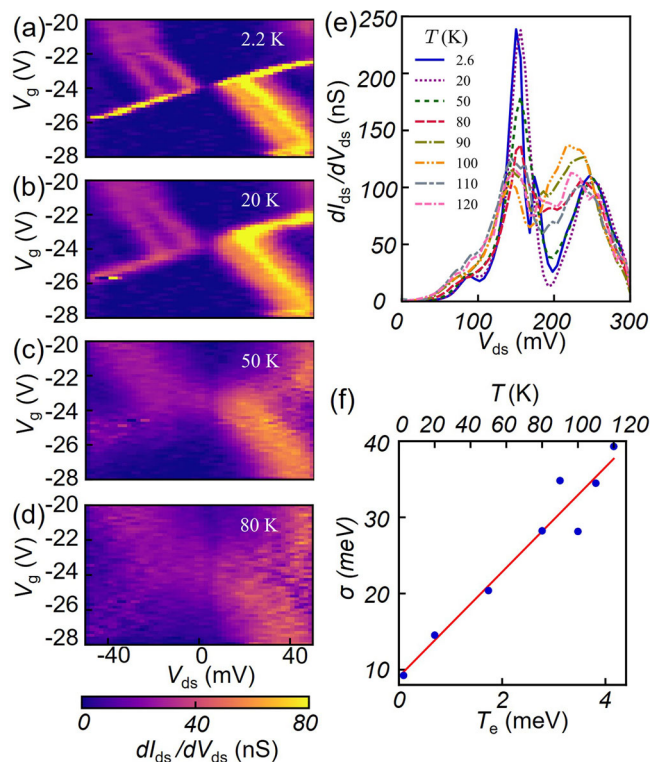


Fig. 5 Temperature dependence of orbital levels and CDs in GNR.

a–d Transport properties of Device 2 were measured at **a** 2.2 K, **b** 20 K, **c** 50 K, and **d** 80 K. **e** Temperature dependence of the differential conductance in Device 2. **f** Extracted widths obtained from Gaussian fitting of the current peak at the excited line located at $V_{sd} = 0.15$ V as a function of temperature (dots). The line shows the linear fit.

temperature of the ES. The largest ΔV_{ds} in our GNR was 129 meV, which clearly differs from previously reported results (10–25 meV), where orbital levels were observed below 4.2 K^{6–13}. Only one report has a similar or higher ΔV_{ds} (300 meV) with a very short GNR (~5 nm) bridged between graphene electrodes²⁹. In this device, an ES was observed even at 75 K³². This structure is similar to that of our GNR, where a very fine structure of GNR is formed within wider GNRs (Fig. 2j), indicating that size is a dominant factor in the stability of the orbital-level spacing in our GNR-QD device. The threshold temperature of 20 K is much higher than that of Si-based QDs (~1 K)²⁹. It has been theoretically predicted that m^* in GNRs is much lower than that in Si³³. This may also be one of the reasons for the high-temperature observations of orbital-level spacing in our GNR-QD devices.

It should be mentioned that although the appearance rate of CD is relatively high (>56%), clear ES observations were rare (below 10%), which can be due to the difficulty of (i) obtaining a single GNR-QD and (ii) increasing the bandgap of GNR-QDs. Further shortening the GNR length and reducing the number of layers of GNR-QDs may be possible approaches to solve these issues, which are the future work of our study toward future applications of GNR-QD-based integrated quantum devices. Uniformity and device-to-device variation should also be discussed for future industrial applications of integrated quantum devices. Previously, most quantum devices comprising nanocarbon materials had very low fabrication yields. Because our study improves the yield up to 56%, it is now feasible to discuss uniformity and device-to-device variation. To address these issues, it is necessary to establish a novel measurement system that can measure many quantum devices within a short time.

This is an important subject for the practical use of integrated quantum devices. To improve uniformity and reduce device-to-device variation, the fabrication process also needs to be improved, similar to current Si-based technology, by scaling up the reaction chamber and improving the uniformity of the plasma source, temperature, gas flow, etc., which is one of the next subjects of our research.

Conclusion

We have demonstrated the scalable fabrication (fabrication yield >56%) of GNR-QD devices by adjusting growth conditions and L_{Ni} . A systematic investigation revealed that very fine structures that formed in the middle of the GNR were possible candidates for QDs. More than 56% of devices showed clear CD features. Detailed measurements of quantum features were also performed, which revealed clear orbital-level spacings between the GS and ES in our GNR-QD device. Furthermore, the orbital levels were stable at relatively high temperatures (~20 K). The scalable fabrication of GNR-QD devices with clear orbital-level spacings at relatively high temperatures have the potential to accelerate the development of GNR-based quantum devices for future applications.

Methods

Device fabrication. Multiple Ni patterns of nanobars, source-drain electrodes, and side-gate electrodes were fabricated using conventional electron beam lithography (ELS-7500, Elionix) and a liftoff process followed by vacuum evaporation of the Ni film (typically 50 nm).

Plasma CVD. A homemade plasma CVD system was used for the GNR synthesis. Before plasma CVD growth, an electric furnace was heated to the desired temperature (typically 800–900 °C) under a flow of hydrogen (50 Pa). A substrate with Ni patterns was transferred to the central area, and rapid heating was performed. CH_4 and H_2 gases (250 Pa) were allowed to flow after reaching a fixed heating time (typically 60 s), during which the Ni nanobars were not dissipated. Subsequently, radiofrequency power (30–60 W, 13.56 MHz) was applied to the coils outside the quartz tube. The plasma irradiation time was typically 5–30 s. Following plasma CVD, the substrate was moved from the center to the outside of the electric furnace to rapidly decrease the temperature of the substrate.

Characterization. The structure of the GNR sample was characterized by scanning electron microscopy (SEM; Hitachi, SU1510, Japan). Electrical measurements of the GNR devices were performed using a vacuum probe station with a semiconductor parameter analyzer (HP 4155 C) from ~15 K to room temperature (15 K system). Further detailed-quantum features were measured using a He-pumping refrigerator, which can decrease the temperature to ~2.2 K (2.2 K system). The devices were mounted on chip carriers and sample holders in a refrigerator. The currents were measured using a semiconductor parameter analyzer and a sensitive current preamplifier (DL 1211).

Data availability

The authors declare that data supporting the findings of this study are available within the article and its supplementary figures, tables, and movie files.

Received: 1 July 2022; Accepted: 13 December 2022;

Published online: 22 December 2022

References

1. Trauzettel, B., Bulaev, D., Loss, D. & Burkard, G. Spin qubits in graphene quantum dots. *Nat. Phys.* **3**, 192 (2007).
2. Min, H. et al. Intrinsic and rashba spin-orbit interactions in graphene sheets. *Phys. Rev. B* **74**, 165310 (2006).
3. Huertas-Hernando, D., Guinea, F. & Brataas, A. Spin-orbit coupling in curved graphene, fullerenes, nanotubes, and nanotube caps. *Phys. Rev. B* **74**, 155426 (2006).
4. Ponomarenko, L. A. et al. Chaotic dirac billiard in graphene quantum dots. *Science* **320**, 356–358 (2008).
5. Stampfer, C. et al. Tunable graphene single electron transistor. *Nano Lett* **8**, 2378–2383 (2008).

6. Schnez, S. et al. Observation of excited states in a graphene quantum dot. *Appl. Phys. Lett.* **94**, 012107-1-3 (2009).
7. Banszerus, L. et al. Single-electron double quantum dots in bilayer graphene. *Nano Lett.* **20**, 2005–2011 (2020).
8. Wang, X. et al. Graphene nanoribbons with smooth edges behave as quantum wires. *Nat. Nanotechnol.* **6**, 563–567 (2011).
9. Gröning, O. et al. Engineering of robust topological quantum phases in graphene nanoribbons. *Nature* **560**, 209–213 (2018).
10. Mishra, S. et al. Topological frustration induces unconventional magnetism in a nanographene. *Nat. Nanotechnol.* **15**, 22–28 (2020).
11. Güttinger, J. et al. Electron-hole crossover in graphene quantum dots. *Phys. Rev. Lett.* **103**, 046810-1-4 (2009).
12. Güttinger, J., Frey, T., Stampfer, C., Ihn, T. & Ensslin, K. Spin states in graphene quantum dots. *Phys. Rev. Lett.* **105**, 116801-1-4 (2010).
13. Volk, C. et al. Probing relaxation times in graphene quantum dots. *Nat. Commun.* **4**, 1753-1-6 (2013).
14. Loss, D. & DiVincenzo, D. P. Quantum computation with quantum dots. *Phys. Rev. A* **57**, 120–126 (1997).
15. Koppens, F. H. L. et al. Driven coherent oscillations of a single electron spin in a quantum dot. *Nature* **442**, 766–771 (2006).
16. Altimiras, C. et al. Tuning energy relaxation along quantum Hall channels. *Phys. Rev. Lett.* **105**, 226804 (2010).
17. Otsuka, T. et al. Fast probe of local electronic states in nanostructures utilizing a single-lead quantum dot. *Sci. Rep.* **5**, 14616-1-9 (2015).
18. Otsuka, T. et al. Higher-order spin and charge dynamics in a quantum dot-lead hybrid system. *Sci. Rep.* **7**, 12201-1-6 (2017).
19. Thierschmann, H. et al. Three-terminal energy harvester with coupled quantum dots. *Nat. Nanotechnol.* **10**, 854–859 (2015).
20. Saraswat, V., Jacobberger, R. M. & Arnold, M. S. Materials science challenges to graphene nanoribbon electronics. *ACS Nano* **15**, 3674–3708 (2021).
21. Wang, H. et al. Graphene nanoribbons for quantum electronics. *Nat. Rev. Phys.* **3**, 791–802 (2021).
22. Petta, J. R. et al. Coherent manipulation of coupled electron spins in semiconductor quantum dots. *Science* **309**, 2180 (2005).
23. Nowack, K. C. et al. Single-shot correlations and two-qubit gate of solid-state spin. *Science* **333**, 1269 (2011).
24. Shulman, M. D. et al. Demonstration of entanglement of electrostatically coupled singlet-triplet qubits. *Science* **336**, 202 (2012).
25. Kato, T. & Hatakeyama, R. Site- and alignment-controlled growth of graphene nanoribbons from nickel nanobars. *Nat. Nanotechnol.* **7**, 651–656 (2012).
26. Suzuki, H. et al. Wafer scale fabrication and growth dynamics of suspended graphene nanoribbon arrays. *Nat. Commun.* **7**, 11797-1-10 (2016).
27. Suzuki, H., Ogura, N., Kaneko, T. & Kato, T., Highly stable persistent photoconductivity with suspended graphene nanoribbons. *Sci. Rep.* **8**, 11819-1-9 (2018).
28. Li, Q.-Y. et al. Enhanced thermoelectric performance of as-grown suspended graphene nanoribbons. *ACS Nano* **13**, 9182–9189 (2019).
29. Yang, C. H. et al. Operation of a silicon quantum processor unit cell above one kelvin. *Nature* **580**, 350–354 (2020).
30. Gehring, P. et al. Distinguishing Lead and Molecule States in Graphene-Based Single-Electron Transistors *ACS Nano* **11**, 5325–5331 (2017).
31. Ono, K., Tanamoto, T. & Ohguro, T. Pseudosymmetric bias and correct estimation of Coulomb/confinement energy for unintentional quantum dot in channel of metal-oxide-semiconductor field-effect transistor. *Appl. Phys. Lett.* **103**, 183107 (2013).
32. Abbassi, M. E. et al. Controlled quantum dot formation in atomically engineered graphene nanoribbon field-effect transistors. *ACS Nano* **14**, 5754–5762 (2020).
33. Raza, H. & Kan, E. C. Armchair graphene nanoribbons: electronic structure and electric-field modulation. *Phys. Rev. B* **77**, 245434-1-5 (2008).

Acknowledgements

This work was supported in part by Scientific Research A (grant no. 19H00664), JSPS Transformative Research Areas (A) “Science of 2.5 Dimensional Materials” program (22H05441), MEXT Leading Initiative for Excellent Young Researchers, Grants-in-Aid for Scientific Research (grant no. 20J14418 and 21K18592) from JSPS KAKENHI, JST-PRESTO (grant no. J170002074 and JPMJPR16N3), JSPS A3 Foresight Program (“2D Materials and van der Waals Heterostructures”), Sumitomo Foundation Fiscal 2021 Grant for Basic Science Research Projects, Yazaki Memorial Foundation for Science and Technology, Mitsubishi Foundation, Takahashi Industrial and Economic Research Foundation Research Grant, The Murata Science Foundation Research Grant, Izumi Science and Technology Foundation Research Grant, Fujikura Foundation Research Grant, and FRiD Tohoku University and the Cooperative Research Project Program of the Research Institute of Electrical Communication, Tohoku University. We thank T. Johmen and RIEC Fundamental Technology Center for fruitful discussions and technical support.

Author contributions

T. Kato and T.O. designed the experiments and supervised the project. T. Kitada, W.O., M.S., and N.S., M. Shinozaki, T. Abe, T. Aizawa, and T. Kumasaka fabricated the devices and performed the measurements. T. Kato, T. Kitada, W.O., T. Otsuka, M. Shinozaki, T. Abe, and Y.M. analyzed the data, and T. Kato, T. Kitada, W.O., T. Otsuka, and T. Kaneko prepared the manuscript. All the authors discussed the results and commented on the manuscript.

Competing interests

The authors declare no competing interests.

Additional information

Supplementary information The online version contains supplementary material available at <https://doi.org/10.1038/s43246-022-00326-3>.

Correspondence and requests for materials should be addressed to Toshiaki Kato or Tomohiro Otsuka.

Peer review information *Communications Materials* thanks Zhenxiang Cheng and the other, anonymous, reviewer(s) for their contribution to the peer review of this work. Primary Handling Editors: Sunkook Kim and Aldo Isidoro.

Reprints and permission information is available at <http://www.nature.com/reprints>

Publisher's note Springer Nature remains neutral with regard to jurisdictional claims in published maps and institutional affiliations.



Open Access This article is licensed under a Creative Commons Attribution 4.0 International License, which permits use, sharing, adaptation, distribution and reproduction in any medium or format, as long as you give appropriate credit to the original author(s) and the source, provide a link to the Creative Commons license, and indicate if changes were made. The images or other third party material in this article are included in the article's Creative Commons license, unless indicated otherwise in a credit line to the material. If material is not included in the article's Creative Commons license and your intended use is not permitted by statutory regulation or exceeds the permitted use, you will need to obtain permission directly from the copyright holder. To view a copy of this license, visit <http://creativecommons.org/licenses/by/4.0/>.

© The Author(s) 2022